

Spatio-Temporal Energy Cascade in Three-Dimensional Magnetohydrodynamic Turbulence

Giuseppe Arrò,¹ Hui Li,¹ and William H. Matthaeus²

¹*Los Alamos National Laboratory, Los Alamos, NM 87545, USA*

²*Department of Physics and Astronomy, University of Delaware, Newark, DE 19716, USA*

We present a new scale decomposition method to investigate turbulence in wavenumber-frequency space. Using 3D magnetohydrodynamic turbulence simulations, we show that magnetic fluctuations with time scales longer than the nonlinear time exhibit an inverse cascade toward even smaller frequencies. Low frequency magnetic fluctuations support turbulence, acting as an energy reservoir that is converted into plasma kinetic energy, the latter cascading toward large wavenumbers and frequencies, where it is dissipated. Our results shed new light on the spatio-temporal properties of turbulence, potentially explaining the origin and role of low frequency turbulent fluctuations in the solar wind.

Turbulence is ubiquitous in space and astrophysical plasmas, including the solar wind (SW) [1], the interstellar medium [2], accretion disks of compact objects [3], and galaxy clusters [4]. The signature of turbulence is the generation of fluctuations with broadband wavenumber and frequency spectra. Turbulent plasmas are typically subject to strong background magnetic fields, inducing a wavenumber anisotropy of the kind $k_{\perp} > k_{\parallel}$ [5–11], with k_{\perp} and k_{\parallel} representing wavenumbers perpendicular and parallel to the magnetic field. Numerical [12–16] and observational [17, 18] SW studies have revealed that plasma turbulence has nontrivial spatio-temporal properties, with a tendency for magnetic field, velocity and density fluctuations to be concentrated at low frequencies ω and small k_{\parallel} . Low (k_{\parallel}, ω) modes are often interpreted as quasi-2D structures, like flux ropes and vortices [19–24], since their energy distribution in $(k_{\perp}, k_{\parallel}, \omega)$ space does not follow the dispersion relation of waves.

The origin of low (k_{\parallel}, ω) turbulent fluctuations has been debated for decades and is still not well understood. Several theoretical explanations for the formation of $(\omega \sim 0, k_{\parallel} \sim 0)$ modes have been proposed, including quasi-2D models of nearly incompressible turbulence [25–27], turbulence driven by counterpropagating Alfvén waves [28, 29], nonlinear frequency broadening of magnetohydrodynamic (MHD) modes [30, 31], and inverse turbulent cascades driven by the conservation of MHD and reduced-MHD invariants [32, 33]. In addition to understanding their origin, the presence of low (k_{\parallel}, ω) modes also raises the question of whether such fluctuations play a role in driving the turbulent cascade, or if they are dynamically irrelevant once generated. Despite the long-standing efforts in addressing these questions, a unifying description for the origin of low (k_{\parallel}, ω) fluctuations and their role in turbulence is still missing.

Understanding the spatio-temporal properties of turbulence has fundamental implications for several space and astrophysical problems. These include the solar corona heating [34, 35], the SW acceleration and expansion [36, 37], the emergence of “1/f” frequency spectra in

the SW [38, 39], the acceleration and transport of cosmic rays [40–42], angular momentum transport in accretion disks [43, 44], the dynamics of molecular clouds and star formation [45, 46], and the turbulent dynamo [47–49].

In this Letter, we present a new framework to study how turbulence reorganizes energy among fluctuations with different wavenumbers and frequencies. We use this method to investigate the origin of low frequency SW turbulent fluctuations, and their role in the turbulent cascade. Our approach employs the coarse graining (CG) technique, frequently used to study hydrodynamic [50–52], MHD [53–55], and plasma turbulence [56–59]. The CG method consists in low-pass filtering the equations of motion of the system, cutting-off small scales. The global energy balance obtained from filtered equations gives a set of quantities describing large scale energy transfers, plus some cascade terms, representing energy exchanges between large and small scales. We apply this method to MHD equations

$$\partial_t \rho + \nabla \cdot (\rho \mathbf{u}) = 0,$$

$$\partial_t (\rho \mathbf{u}) + \nabla \cdot (\rho \mathbf{u} \mathbf{u}) = -\nabla P + \mathbf{J} \times \mathbf{B} + \nabla \cdot \mathbf{\Pi} + \mathbf{F}_u, \quad (1)$$

$$\partial_t \mathbf{B} = \nabla \times (\mathbf{u} \times \mathbf{B} - \eta \mathbf{J}) + \mathbf{F}_B,$$

where ρ , \mathbf{u} and P are the plasma density, velocity and pressure. \mathbf{B} is the magnetic field, $\mathbf{J} = \nabla \times \mathbf{B}$, η is the magnetic diffusivity. $\mathbf{\Pi} = \rho \nu [\nabla \mathbf{u} + \nabla \mathbf{u}^T - (2/3)(\nabla \cdot \mathbf{u})\mathbf{I}]$ is the viscous stress tensor, where ν is the viscosity, \mathbf{I} is the identity matrix, and T indicates the transpose operation. \mathbf{F}_u and \mathbf{F}_B are large scale turbulent forcing terms.

The CG method typically involves only spatial scales, but we extend the technique by introducing the spatio-temporal low-pass filter

$$\bar{q}(\mathbf{x}, t, \mathbf{k}, \tau) = \sum_{\mathbf{k}' < \mathbf{k}} \int dt' Q(\mathbf{k}', t') e^{i\mathbf{k}' \cdot \mathbf{x}} G_{\tau}(t-t'), \quad (2)$$

where $q(\mathbf{x}, t)$ is a generic quantity with spatial Fourier transform $Q(\mathbf{k}, t)$, and G_{τ} is a boxcar function with width τ . \bar{q} contains wavenumbers $< \mathbf{k}$ and time scales $>$

τ . The corresponding density-weighted filter is $\hat{q} = \overline{\rho q} / \bar{\rho}$ [60]. By applying this filter to Eqs. (1), and calculating the global energy balance, we obtain:

$$\begin{aligned} \partial_t \left\langle \frac{1}{2} \bar{\rho} \hat{u}^2 \right\rangle &= -W_P - \Pi_u + W_{e.m.} - D_u + I_u, \\ \partial_t \left\langle \frac{1}{2} \bar{B}^2 \right\rangle &= -\Pi_B - W_{e.m.} - D_B + I_B, \end{aligned} \quad (3)$$

where $\langle \cdot \rangle$ indicates the spatial average over the system size, and we assumed no transport across the system boundaries, causing all terms in the form of a divergence to vanish when averaged (as in periodic systems). A detailed derivation of Eqs. (3) is provided in Supplemental Material. The energy transfer channels (ETCs) in Eqs. (3) are

$$\begin{aligned} I_B &= \langle \bar{\mathbf{F}}_B \cdot \bar{\mathbf{B}} \rangle, \quad I_u = \langle \bar{\mathbf{F}}_u \cdot \hat{\mathbf{u}} \rangle, \\ W_{e.m.} &= \langle -(\hat{\mathbf{u}} \times \bar{\mathbf{B}}) \cdot \bar{\mathbf{J}} \rangle, \quad \Pi_B = \langle \bar{\boldsymbol{\tau}}_E \cdot \bar{\mathbf{J}} \rangle, \\ \Pi_u &= \Pi_u^S + \Pi_u^L = \langle -\bar{\rho} \bar{\boldsymbol{\tau}}_u \cdot \nabla \hat{\mathbf{u}} \rangle + \langle -\bar{\boldsymbol{\tau}}_B \cdot \hat{\mathbf{u}} \rangle, \end{aligned} \quad (4)$$

$$W_P = \langle -\bar{P} \nabla \cdot \hat{\mathbf{u}} \rangle, \quad D_B = \langle \eta \bar{\mathbf{J}}^2 \rangle, \quad D_u = \langle \bar{\boldsymbol{\Pi}} \cdot \nabla \hat{\mathbf{u}} \rangle,$$

with I_B and I_u representing the magnetic and kinetic energy injection rates, $W_{e.m.}$ and W_P are the electromagnetic (e.m.) and pressure works, D_B and D_u are the magnetic and kinetic energy dissipation rates, all representing energy exchanges at scales $< \mathbf{k}$ and $> \tau$. Π_B and Π_u are the magnetic and kinetic energy cascade rates, quantifying energy transfers from scales $< \mathbf{k}$ and $> \tau$, to scales $> \mathbf{k}$ and $< \tau$. $\boldsymbol{\tau}_u = (\widehat{\mathbf{u}\mathbf{u}} - \widehat{\mathbf{u}\hat{\mathbf{u}}})$ is the subscale stress tensor [61], while $\boldsymbol{\tau}_E = -(\widehat{\mathbf{u}} \times \bar{\mathbf{B}} - \hat{\mathbf{u}} \times \bar{\mathbf{B}})$ and $\boldsymbol{\tau}_B = (\bar{\mathbf{J}} \times \bar{\mathbf{B}} - \bar{\mathbf{J}} \times \bar{\mathbf{B}})$ are the subscale electric field and Lorentz force. Subscale terms couple small scales to large scales. Hence, Π_B represents the interaction between small scale electric fields $\boldsymbol{\tau}_E$ and large scale currents $\bar{\mathbf{J}}$. Π_u includes two contributions: Π_u^S quantifies the interaction between small scale stresses $\boldsymbol{\tau}_u$ and the large scale strain tensor $\nabla \hat{\mathbf{u}}$; Π_u^L couples the small scale Lorentz force $\boldsymbol{\tau}_B$ to large scale velocities $\hat{\mathbf{u}}$.

We apply our CG method to a 3D simulation of MHD turbulence, realized with *Athena++* [62], implementing Eqs. (1). We consider a uniform periodic grid with 256×512^2 points, and size $L_z = 3L_y = 3L_x = 6\pi$ (in arbitrary units L_0). The plasma has zero initial velocity, homogeneous density ρ_0 and guide field $\mathbf{B}_0 = B_0 \hat{\mathbf{z}}$. Pressure is isothermal, with plasma beta $\beta = 2c_s^2/c_A^2 = 0.5$, where c_s and $c_A = B_0/\sqrt{\rho_0}$ are the sound and Alfvén speeds. Turbulence is driven by \mathbf{F}_u and \mathbf{F}_B , consisting of sinusoidal perturbations with wavenumbers $1 \leq k_{\parallel}/k_{\parallel,0} \leq 3$ and $1 \leq k_{\perp}/k_{\perp,0} \leq 4$ (where $k_{\parallel,0} = 2\pi/L_z$ and $k_{\perp,0} = 2\pi/L_x$). Each perturbation evolves in time following the Langevin antenna (LA) scheme [63], with driving frequency $\omega_0 = 0.8 \tau_A^{-1}$ and decorrelation rate $\gamma_0 = -0.7 \tau_A^{-1}$

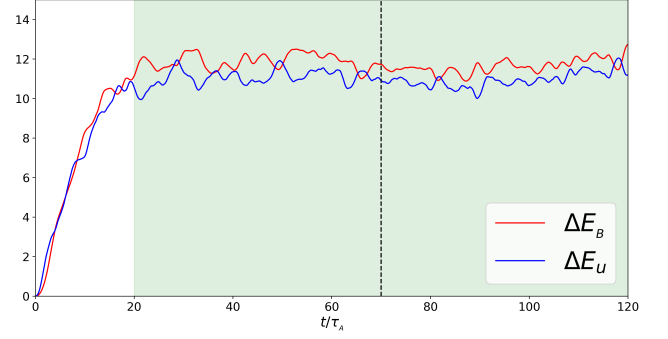


FIG. 1. Temporal evolution of magnetic and kinetic energy variations ΔE_B and ΔE_u . The green shaded area indicates the time interval used for the space-time analysis.

(where $\tau_A = L_0/c_A$). \mathbf{F}_u and \mathbf{F}_B are solenoidal and perpendicular to \mathbf{B}_0 , driving incompressible Alfvénic perturbations with cross helicity $\sigma_C \simeq 0$. \mathbf{F}_u and \mathbf{F}_B are set to induce magnetic and velocity fluctuations with root mean square (rms) amplitudes $\delta B_{rms}/B_0 \simeq 0.18$ and $\delta u_{rms}/c_A \simeq 0.17$. Our setup produces turbulence with typical near-Earth SW parameters [64]. We set $\eta = \nu = 2.5 \cdot 10^{-4}$ (in L_0^2/τ_A units).

Figure 1 shows the temporal evolution of magnetic and kinetic energy variations, $\Delta E_B = E_B(t) - E_B(0)$ and $\Delta E_u = E_u(t) - E_u(0)$ (in $\rho_0 c_A^2 L_0^3$ units). Both energies quickly grow and saturate, after $20 \tau_A$. We consider interval $T = [20 \tau_A, 120 \tau_A]$ for our analysis (green shaded area), when turbulence is fully developed and nearly stationary. Figures 2(a)-(b) show (k_{\parallel}, ω) and (k_{\perp}, ω) projections of the magnetic field space-time Fourier spectrum P_B , calculated over interval T , with simulation data sampled every $\Delta t = 0.1 \tau_A$. (k_{\parallel}, ω) and (k_{\perp}, ω) projections are calculated as $P_B(k_{\parallel}, \omega) = \int P_B(k_{\perp}, k_{\parallel}, \omega) dk_{\perp}$ and $P_B(k_{\perp}, \omega) = \int P_B(k_{\perp}, k_{\parallel}, \omega) dk_{\parallel}$. The corresponding projections of the velocity spectrum P_u are shown in Fig. 2(c)-(d). We see that energy is distributed into concentric shells in (k_{\parallel}, ω) space, quickly falling off toward large k_{\parallel} and ω . (k_{\perp}, ω) projections also show that most energy is concentrated around small ω , but with a wider distribution in k_{\perp} , up to relatively high wavenumbers. Despite our turbulent driver being incompressible, density fluctuations still develop, reaching an rms amplitude of $\delta \rho_{rms}/\rho_0 \simeq 0.08$ at fully developed turbulence. Figures 2(e)-(f) show (k_{\parallel}, ω) and (k_{\perp}, ω) projections of the density spectrum P_ρ . Similarly to magnetic and velocity fluctuations, density fluctuations are concentrated around low ω , exhibiting a strong $k_{\perp} > k_{\parallel}$ anisotropy. Overall, (k, ω) spectra of magnetic, velocity and density fluctuations do not follow the dispersion relations (dashed lines) of Alfvén waves (AW), slow modes (SM), and fast modes (FM), with most energy stored in low ω , low k_{\parallel} fluctuations, consistently with previous numerical works [16] and SW observations [18].

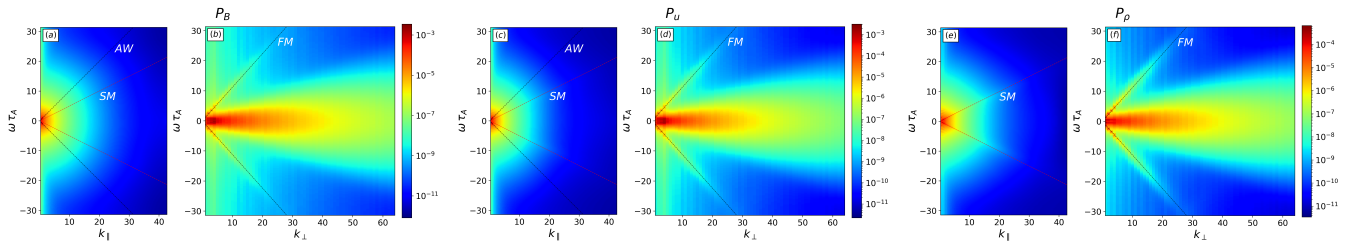


FIG. 2. (k_{\parallel}, ω) and (k_{\perp}, ω) projections of magnetic field, velocity and density spectra P_B (a)-(b), P_u (c)-(d), and P_{ρ} (e)-(f). Dashed lines indicate the dispersion relations of Alfvén wave (AW) and slow modes (SM) for parallel propagation ($k_{\perp}=0$), and of fast modes (FM) for perpendicular propagation ($k_{\parallel}=0$).

We investigate the origin of such spectral features using our spatio-temporal CG method, tracking energy transfers from injection to dissipation in $(k_{\perp}, k_{\parallel}, \tau)$ space (with $\tau \simeq 2\pi/\omega$). The goal is understanding how low ω (large τ) fluctuations develop, and their role in the turbulent cascade. We analyze two projections of ETCs in Eqs. 4: (k_{\parallel}, τ) projections are obtained by filtering in k_{\parallel} and τ , retaining all k_{\perp} ; (k_{\perp}, τ) projections are calculated by filtering in k_{\perp} and τ , keeping all k_{\parallel} . For the temporal filtering, we center the boxcar kernel G_{τ} at $t=70\tau_A$ (vertical dashed line in Fig. 1), varying its width τ from $0.2\tau_A$ to $100\tau_A$, covering the whole interval T . ETCs are shown in Fig. 3, with black lines indicating their isocontours. As I_B and I_u exhibit analogous $(k_{\perp}, k_{\parallel}, \tau)$ dependence and comparable amplitude, we analyze the total energy injection rate $I_{tot}=I_B+I_u$. For the same reason, we show the total dissipation rate $D_{tot}=D_B+D_u$. I_B , I_u , D_B and D_u are shown separately in Supplemental Material. For each ETCs, both (k_{\parallel}, τ) and (k_{\perp}, τ) projections exhibit the same qualitative features, but they are not isotropic in $(k_{\parallel}, k_{\perp})$ space. The ETCs anisotropy causes the $k_{\perp} > k_{\parallel}$ anisotropy observed in spectra [65, 66]. As a reference, we show the parallel and perpendicular integral scales k_{\parallel}^{int} and k_{\perp}^{int} (vertical green dashed lines) [67]

$$(k_{\perp}^{int}, k_{\parallel}^{int}) = \frac{\int \int \int (k_{\perp}, k_{\parallel}) P_u dk_{\perp} dk_{\parallel} d\omega}{\int \int \int P_u dk_{\perp} dk_{\parallel} d\omega}, \quad (5)$$

representing the scale of energy containing fluctuations, and the nonlinear time (horizontal green dashed lines) $\tau_{nl} = 2\pi/(k_{\perp}^{int} \delta u_{rms})$. Starting from I_{tot} , Fig. 3(a)-(b), we see it is positive and increases with wavenumber, up to $k_{\parallel} \simeq 1.3$ and $k_{\perp} \simeq 6$, after which it saturates, indicating no contribution from larger wavenumbers. Regarding its τ dependence, we note that I_{tot} is not peaked at the driving time $2\pi/\omega_0 \simeq 7.8\tau_A$, but exhibits a broad frequency response, growing from $\tau \simeq 15$ to $\tau \simeq 1.5$, while being almost constant elsewhere. This broadening is determined by the decorrelation rate γ_0 of the LA driver, typically chosen to be slightly smaller than ω_0 . Different drivers may alter the (k, ω) distribution of injected perturbations, but we choose the LA approach since it has

been proven to successfully reproduce key features of SW turbulence [63, 68].

Energy injected by I_{tot} is transferred to other scales by the cascade terms Π_B and Π_u . Starting from Π_B , Fig. 3(c)-(d), we find it is negative for $\tau \gtrsim \tau_{nl}$ and wavenumbers larger than k_{\parallel}^{int} and k_{\perp}^{int} , while being positive for $\tau < \tau_{nl}$, where it peaks around integral scales. This indicates a frequency space bifurcation in the magnetic energy cascade, with large τ (low ω) fluctuations exhibiting an inverse cascade¹ toward even lower frequencies and smaller wavenumbers in (k, τ) space, while small τ (high ω) magnetic modes undergo a direct cascade, with the cascade rate being stronger around k_{\parallel}^{int} and k_{\perp}^{int} , in the inertial range. Hence, part of the injected magnetic energy is transferred to low (k, ω) fluctuations, while another fraction is transferred to high (k, ω) modes. We first follow the path taken by low ω magnetic fluctuations. Magnetic energy piling up at large τ because of the inverse cascade can be converted into kinetic energy by $W_{e.m.}$. Figures 3(e)-(f) show that $W_{e.m.}$ is positive in the same range where Π_B is negative, for $\tau \gtrsim \tau_{nl}$ and wavenumbers larger than k_{\parallel}^{int} and k_{\perp}^{int} , and their absolute magnitudes are similar, indicating that low ω magnetic energy is converted into low ω kinetic energy. Such balance between the inverse magnetic energy cascade and a low ω energy sink, $W_{e.m.}$ in this case, is expected and has to occur in order for turbulence to reach a quasi-stationary state. The combination of the inverse magnetic energy cascade and the magnetic-to-kinetic energy conversion at low ω , implies an accumulation of magnetic and kinetic energy at small frequencies, explaining the origin of low ω fluctuations in energy spectra. Unlike Π_B , the kinetic energy cascade rate Π_u , Fig. 3(g)-(h), is positive at all (k, τ) scales, peaking around integral scales and at τ slightly smaller than τ_{nl} , indicating a direct kinetic energy cascade, regardless of the frequency.

¹ By “inverse cascade” we mean energy transfer from high to low frequencies. Other aspects typically associated with the traditional concept of “cascade”, such as its locality, are not addressed here and will be investigated in future studies.

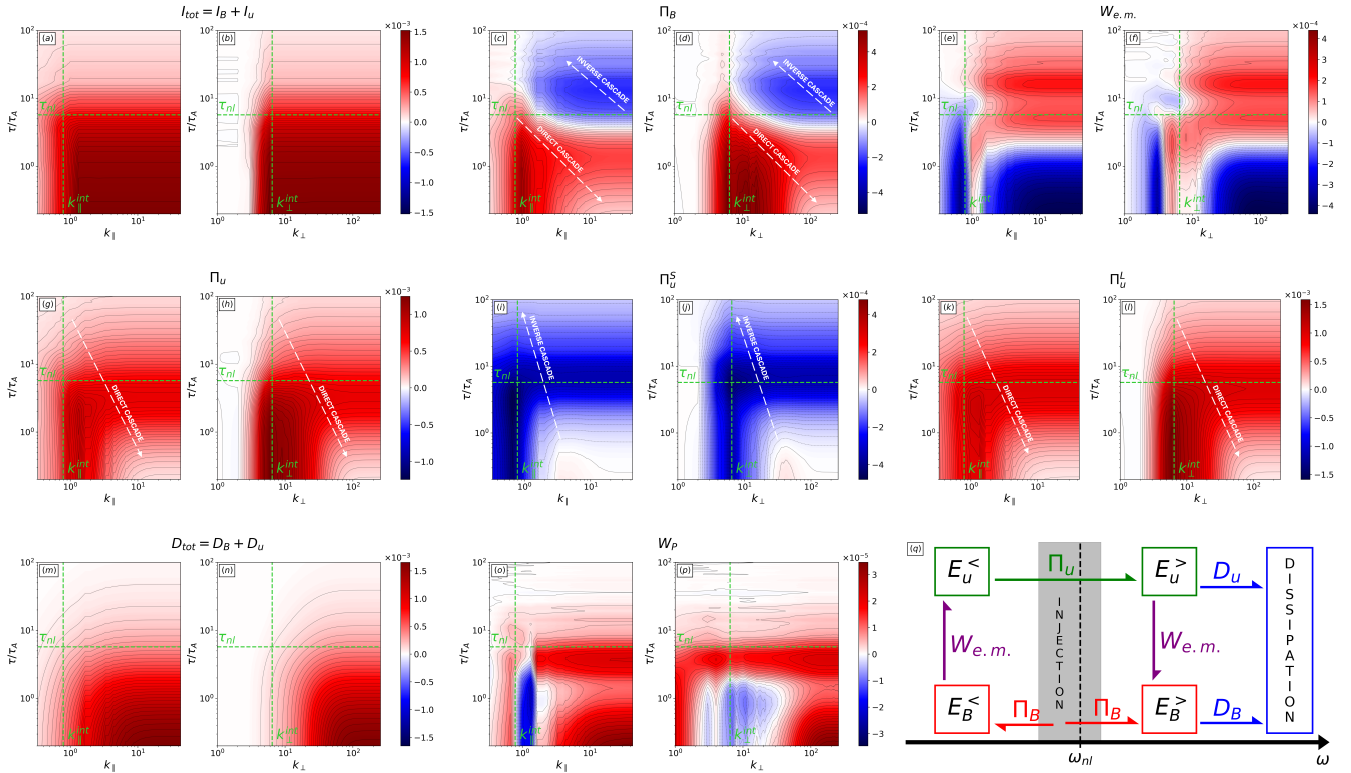


FIG. 3. (k_{\parallel}, τ) and (k_{\perp}, τ) projections of $I_B + I_u$ (a)-(b), Π_B (c)-(d), $W_{e.m.}$ (e)-(f), Π_u (g)-(h), Π_u^S (i)-(j), Π_u^L (k)-(l), $D_B + D_u$ (m)-(n), and W_P (o)-(p), with vertical green dashed lines indicating parallel and perpendicular integral scales k_{\parallel}^{int} and k_{\perp}^{int} , while horizontal green dashed lines represent the nonlinear time τ_{nl} . Schematic representation of the energy cascade in frequency space (q).

Combining Π_B , $W_{e.m.}$ and Π_u , we thus find that low ω magnetic fluctuations contribute to driving turbulence, providing magnetic energy that is first converted into low ω kinetic energy by $W_{e.m.}$, and finally transferred to higher (k, ω) fluctuations by Π_u . Since $W_{e.m.}$ is negative for large k and small τ , Fig. 3(e)-(f), part of the small scale kinetic energy resulting from the direct cascade is converted to small scale magnetic energy.

Additional insights on the turbulent cascade are obtained decomposing Π_u into Π_u^S and Π_u^L , in Fig. 3(i)-(l). We find that Π_u^S is negative over most of $(k_{\perp}, k_{\parallel}, \tau)$ space (except at small scales, where it is weakly positive), indicating an inverse cascade. This is strikingly different from hydrodynamic turbulence, where Π_u^S is typically positive, being the only cascade term [69]. Conversely, Π_u^L is positive at all scales, and stronger in amplitude than Π_u^S , thus producing a net direct kinetic energy cascade when combined with Π_u^S . Hence, the direct kinetic energy cascade in MHD turbulence is mainly driven by e.m. interactions between the small scale Lorentz force and large scale velocities, quantified by Π_u^L , while the hydrodynamic cascade term Π_u^S opposes the direct Π_u^L cascade.

Magnetic and kinetic energy cascading to small scales

is eventually dissipated. Figures 3(m)-(n) show the dissipation rate D_{tot} to be weak at large scales, growing to large positive values toward high k and small τ , indicating that dissipation mainly affects high frequencies and wavenumbers. Consequently, low ω fluctuations resulting from the inverse cascade are not dissipated. Turbulent SW dissipation is mainly caused by kinetic processes [70], rather than by collisional resistive and viscous effects as in our simulation. However, kinetic scale dissipation is typically mediated by wave-particle interactions [71] and fast intermittent events, like magnetic reconnection [72, 73], whose time scales are comparable to particle gyroperiods. Hence, we expect kinetic effects not to affect the dynamics of low ω fluctuations, whose time scales are much larger than particle gyroperiods [18].

Another channel for kinetic energy dissipation is W_P , quantifying compressible effects. Figures 3(o)-(p) show W_P to be negligibly small for $\tau > \tau_{nl}$, meaning that low ω fluctuations are essentially incompressible, while for $\tau \lesssim \tau_{nl}$ it is negative around integral scales (dilatation), and positive (compression) elsewhere. However, W_P is about one order of magnitude smaller than other ETCs, providing negligible contributions to the global energy balance, consistently with previous studies [55].

The interplay among all ECTs in frequency space is schematically summarized in Fig. 3(q), highlighting the origin and role of low ω turbulent fluctuations. Energy injection is represented by the gray shaded area around the nonlinear frequency $\omega_{nl} \simeq 2\pi/\tau_{nl}$. Part of the injected magnetic energy exhibits an inverse cascade, driven by Π_B , causing a pileup of low ω magnetic energy $E_B^<$, and thus of low ω magnetic fluctuations. Low ω magnetic energy is transferred to low ω kinetic energy $E_u^<$ by the e.m. work $W_{e.m.}$, producing low ω velocity fluctuations. Low ω kinetic energy undergoes a direct cascade, driven by Π_u , toward high ω kinetic energy $E_u^>$. Energy flows into high ω magnetic energy $E_B^>$ through two paths: a direct cascade from injection to $E_B^>$, driven by Π_B , and the kinetic-to-magnetic energy transfer driven by $W_{e.m.}$ at high ω , converting $E_u^>$ into $E_B^>$. Finally, $E_B^>$ and $E_u^>$ are dissipated by D_B and D_u , respectively. $E_B^<$ and $E_u^<$ are not affected by resistive and viscous dissipation, making low ω magnetic field and velocity fluctuations a stable reservoir of energy that contributes to driving the turbulent cascade. The fact that dissipation is efficient at high ω , while not affecting low ω , explains the energy distribution observed in magnetic field and velocity spectra, where most energy lies in low ω modes, while high ω fluctuations are dissipated, exhibiting a negligible energy content.

The main new mechanism unveiled by our spatio-temporal CG analysis is the frequency space bifurcation in the magnetic energy cascade, with magnetic fluctuations exhibiting an inverse cascade at frequencies $\omega < \omega_{nl}$, and a direct cascade for $\omega > \omega_{nl}$. Our results potentially explain the origin of low frequency turbulent fluctuations observed in the SW, showing that low ω modes are not just a passive product of turbulence, but they also support the energy cascade. Additional elements may contribute to low frequency SW fluctuations, as the presence of long-lived structures originating in the solar chromosphere or corona, later advected into the SW. Nevertheless, our analysis shows that turbulence alone is capable of producing low frequency fluctuations locally, suggesting they may develop in-situ in the SW. Here by “low frequency fluctuations” we mean the low ω range in (k, ω) spectra in Fig. 2, also measured in the SW [17, 18]. However, low frequency SW fluctuations cover a wide frequency range, often exhibiting $1/f$ spectra extending about two decades below the turbulence correlation frequency. Such a ω range is only partially accessible in our simulation, as the largest time scales we resolve are about one order of magnitude larger than τ_{nl} .

Our findings have potential implications for the development of new models of plasma turbulence, including frequency information. The inverse magnetic energy cascade we observe is fundamentally different from the turbulent dynamo. In dynamo configurations, small scale low amplitude magnetic perturbations are amplified and grow in size due to field line stretching induced by large

scale hydrodynamic flows, with a wide scale separation between velocity and magnetic fluctuations [47]. This is not the case in our simulation, since both magnetic and velocity perturbations are injected in the same range of scales, with similar amplitudes, mimicking SW turbulence driven by large scale Alfvénic fluctuations. In this scenario, we find that magnetic fluctuations with different ω contribute differently to turbulence, with a fraction of them exhibiting an inverse cascade, while others undergo a direct cascade.

The turbulent cascade may be influenced by several parameters, including β and σ_C [74–76]. To test the generality of our findings, we applied our CG analysis to other two MHD simulations of turbulence, a ($\beta = 18$, $\sigma_C \simeq 0$) run, representing SW turbulence in the outer heliosphere [77], and a ($\beta = 0.5$, $\sigma_C \simeq 0.73$) run, reproducing near-Sun SW turbulence, where σ_C reaches large values (imbalanced turbulence), as measured by Parker Solar Probe [78]. In both runs, the energy cascade exhibits the same spatio-temporal behavior observed in our main ($\beta = 0.5$, $\sigma_C \simeq 0$) run. Specifically, an inverse magnetic energy cascade occurs at $\tau \gtrsim \tau_{nl}$, with magnetic energy being converted into kinetic energy by $W_{e.m.}$ at low ω , complemented by a direct kinetic energy cascade from low to high frequencies (see Supplemental Material). Another parameter that may influence the cascade dynamics is the magnetic helicity σ_B , a conserved MHD quantity undergoing an inverse cascade in wavenumber space [79, 80]. The random phase nature of our magnetic driver \mathbf{F}_B implies the injection of magnetic fluctuations with $\sigma_B \simeq 0$, so we argue that the inverse magnetic energy cascade we observe is not related to the inverse σ_B cascade.

We have shown that low ω magnetic and velocity modes are also associated with density fluctuations, while being nearly incompressible. The question remains to understand the identity of such low ω incompressible structures. A possible interpretation is that low ω fluctuations correspond to long-lived flux ropes, typically observed in the SW, where magnetic pressure is balanced by density (and thus pressure) variations [81–83]. Investigating the properties of low ω turbulent fluctuations in terms of their real space structure will be the subject of future studies.

G. A. acknowledges useful discussions with Prof. Fabio Bacchini, regarding the implementation of the turbulent forcing and other MHD numerical methods. H.L. acknowledges the support by LANL/LDRD program and DOE FES program.

This research is supported by the NASA grant No. 80NSSC23K0101. Opinions, findings, and conclusions expressed in this work are those of the authors and do not necessarily reflect the views of NASA.

Numerical simulations and data analysis have been performed on Perlmutter at NERSC (USA), under the

FES-ERCAP-m4239 project. This research used resources provided by the Los Alamos National Laboratory Institutional Computing Program, which is supported by the U.S. Department of Energy National Nuclear Security Administration under Contract No. 89233218CNA000001.

Supplemental Material

Coarse grained magnetohydrodynamic equations

This section provides a detailed derivation of the spatio-temporal coarse grained magnetohydrodynamic (MHD) equations employed in the Letter.

We introduce a space-time low-pass filter defined as

$$\bar{q}(\mathbf{x}, t, \mathbf{k}, \tau) = \sum_{\mathbf{k}' < \mathbf{k}} \int dt' Q(\mathbf{k}', t') e^{i\mathbf{k}' \cdot \mathbf{x}} G_\tau(t-t'), \quad (6)$$

where $q(\mathbf{x}, t)$ is a generic quantity with spatial Fourier transform $Q(\mathbf{k}, t)$, and G_τ is a boxcar function with width τ . The filtered quantity \bar{q} contains fluctuations with wavenumbers $< \mathbf{k}$ and time scales $> \tau$. The corresponding density-weighted filter is $\hat{q} = \bar{q}/\bar{\rho}$. We consider the MHD equations

$$\partial_t \rho + \nabla \cdot (\rho \mathbf{u}) = 0,$$

$$\partial_t (\rho \mathbf{u}) + \nabla \cdot (\rho \mathbf{u} \mathbf{u}) = -\nabla P + \mathbf{J} \times \mathbf{B} + \nabla \cdot \mathbf{\Pi} + \mathbf{F}_u, \quad (7)$$

$$\partial_t \mathbf{B} = \nabla \times (\mathbf{u} \times \mathbf{B} - \eta \mathbf{J}) + \mathbf{F}_B,$$

with ρ , \mathbf{u} and P indicating the plasma density, velocity and pressure. \mathbf{B} is the magnetic field, $\mathbf{J} = \nabla \times \mathbf{B}$, η is the magnetic diffusivity. $\mathbf{\Pi} = \rho \nu [\nabla \mathbf{u} + \nabla \mathbf{u}^T - (2/3)(\nabla \cdot \mathbf{u})\mathbf{I}]$ is the viscous stress tensor, with ν being the viscosity, \mathbf{I} is the identity matrix, and T indicates the transpose operation. \mathbf{F}_u and \mathbf{F}_B are large scale turbulent forcing terms.

By applying the low-pass filter in Eq. 6 to Eqs. 7, we obtain

$$\partial_t \bar{\rho} + \nabla \cdot (\bar{\rho} \hat{\mathbf{u}}) = 0,$$

$$\partial_t (\bar{\rho} \hat{\mathbf{u}}) + \nabla \cdot (\bar{\rho} \hat{\mathbf{u}} \hat{\mathbf{u}}) = -\nabla \bar{P} + \overline{\mathbf{J} \times \mathbf{B}} + \nabla \cdot \overline{\mathbf{\Pi}} + \overline{\mathbf{F}}_u, \quad (8)$$

$$\partial_t \overline{\mathbf{B}} = \nabla \times (\overline{\mathbf{u} \times \mathbf{B}}) - \eta \nabla \times \overline{\mathbf{J}} + \overline{\mathbf{F}}_B.$$

The strategy now is expressing Eqs. 8 in terms of the low-pass filtered quantities $\bar{\rho}$, $\hat{\mathbf{u}}$ and $\overline{\mathbf{B}}$, plus some sub-scale terms. While the continuity equation is already in the correct form, the momentum and induction equations need some simple algebraic manipulation. To this end, we introduce

$$\hat{\mathbf{u}} \hat{\mathbf{u}} = \hat{\mathbf{u}} \hat{\mathbf{u}} + (\hat{\mathbf{u}} \hat{\mathbf{u}} - \hat{\mathbf{u}} \hat{\mathbf{u}}) = \hat{\mathbf{u}} \hat{\mathbf{u}} + \tau_u,$$

$$\overline{\mathbf{J} \times \mathbf{B}} = \overline{\mathbf{J} \times \mathbf{B}} + (\overline{\mathbf{J} \times \mathbf{B}} - \overline{\mathbf{J} \times \mathbf{B}}) = \overline{\mathbf{J} \times \mathbf{B}} + \tau_B, \quad (9)$$

$$\overline{\mathbf{u} \times \mathbf{B}} = \hat{\mathbf{u}} \times \overline{\mathbf{B}} + (\overline{\mathbf{u} \times \mathbf{B}} - \hat{\mathbf{u}} \times \overline{\mathbf{B}}) = \hat{\mathbf{u}} \times \overline{\mathbf{B}} - \tau_E,$$

where τ_u , τ_B and τ_E are the subscale stress tensor, Lorentz force, and electric field. The momentum equation thus becomes

$$\begin{aligned} \partial_t (\bar{\rho} \hat{\mathbf{u}}) + \nabla \cdot (\bar{\rho} \hat{\mathbf{u}} \hat{\mathbf{u}}) &= -\nabla \bar{P} + \overline{\mathbf{J} \times \mathbf{B}} + \\ &- \nabla \cdot (\bar{\rho} \tau_u) + \tau_B + \nabla \cdot \overline{\mathbf{\Pi}} + \overline{\mathbf{F}}_u, \end{aligned} \quad (10)$$

while the induction equation becomes

$$\partial_t \overline{\mathbf{B}} = \nabla \times (\hat{\mathbf{u}} \times \overline{\mathbf{B}}) - \nabla \times \tau_E - \eta \nabla \times \overline{\mathbf{J}} + \overline{\mathbf{F}}_B. \quad (11)$$

Equations for the low-pass filtered kinetic and magnetic energies are obtained by taking the dot product of Eq. 10 with $\hat{\mathbf{u}}$, and of Eq. 11 with $\overline{\mathbf{B}}$, which gives

$$\begin{aligned} \partial_t \left\langle \frac{1}{2} \bar{\rho} \hat{u}^2 \right\rangle + \nabla \cdot \left\langle \frac{1}{2} \bar{\rho} \hat{u}^2 \hat{\mathbf{u}} \right\rangle &= -\nabla \bar{P} \cdot \hat{\mathbf{u}} + \\ &- (\hat{\mathbf{u}} \times \overline{\mathbf{B}}) \cdot \overline{\mathbf{J}} - [\nabla \cdot (\bar{\rho} \tau_u)] \cdot \hat{\mathbf{u}} + \tau_B \cdot \hat{\mathbf{u}} + \\ &+ (\nabla \cdot \overline{\mathbf{\Pi}}) \cdot \hat{\mathbf{u}} + \overline{\mathbf{F}}_u \cdot \hat{\mathbf{u}}, \end{aligned} \quad (12)$$

$$\begin{aligned} \partial_t \left\langle \frac{1}{2} \overline{B}^2 \right\rangle - \nabla \cdot [(\hat{\mathbf{u}} \times \overline{\mathbf{B}}) \times \overline{\mathbf{B}}] &= (\hat{\mathbf{u}} \times \overline{\mathbf{B}}) \cdot \overline{\mathbf{J}} + \\ &- (\nabla \times \tau_E) \cdot \overline{\mathbf{B}} - \eta (\nabla \times \overline{\mathbf{J}}) \cdot \overline{\mathbf{B}} + \overline{\mathbf{F}}_B \cdot \overline{\mathbf{B}}. \end{aligned}$$

The global energy balance is finally obtained by averaging Eqs. 12 over the system size, which gives

$$\begin{aligned} \partial_t \left\langle \frac{1}{2} \bar{\rho} \hat{u}^2 \right\rangle + J_u &= -W_P - \Pi_u + W_{e.m.} + \\ &- D_u + I_u, \end{aligned} \quad (13)$$

$$\partial_t \left\langle \frac{1}{2} \overline{B}^2 \right\rangle + J_B = -\Pi_B - W_{e.m.} - D_B + I_B,$$

where $\langle \cdot \rangle$ indicates the spatial average, and energy transfer channels are

$$\begin{aligned} J_u &= \left\langle \nabla \cdot \left(\frac{1}{2} \bar{\rho} \hat{u}^2 \hat{\mathbf{u}} \right) \right\rangle, \quad W_P = \langle \nabla \bar{P} \cdot \hat{\mathbf{u}} \rangle, \\ \Pi_u &= \langle [\nabla \cdot (\bar{\rho} \tau_u)] \cdot \hat{\mathbf{u}} - \tau_B \cdot \hat{\mathbf{u}} \rangle, \\ I_u &= \langle \overline{\mathbf{F}}_u \cdot \hat{\mathbf{u}} \rangle, \quad D_u = \langle -(\nabla \cdot \overline{\mathbf{\Pi}}) \cdot \hat{\mathbf{u}} \rangle, \\ J_B &= \left\langle -\nabla \cdot [(\hat{\mathbf{u}} \times \overline{\mathbf{B}}) \times \overline{\mathbf{B}}] \right\rangle, \end{aligned} \quad (14)$$

$$W_{e.m.} = \langle -(\hat{\mathbf{u}} \times \overline{\mathbf{B}}) \cdot \overline{\mathbf{J}} \rangle, \quad \Pi_B = \langle (\nabla \times \tau_E) \cdot \overline{\mathbf{B}} \rangle,$$

$$I_B = \langle \overline{\mathbf{F}}_B \cdot \overline{\mathbf{B}} \rangle, \quad D_B = \langle \eta (\nabla \times \overline{\mathbf{J}}) \cdot \overline{\mathbf{B}} \rangle.$$

If we assume no energy transport across the system boundaries, or if the system is periodic, the kinetic and magnetic energy fluxes J_u and J_B vanish, while other

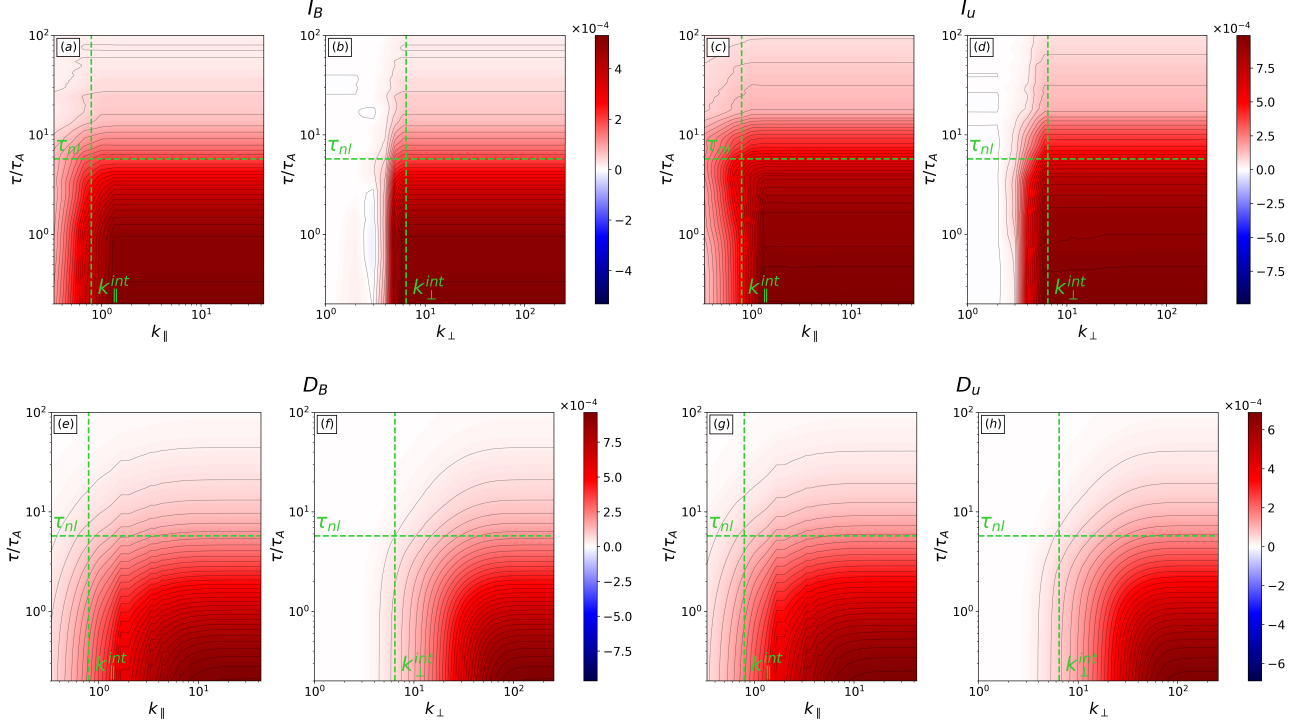


FIG. 4. (k_{\parallel}, τ) and (k_{\perp}, τ) projections of I_B (a)-(b), I_u (c)-(d), D_B (e)-(f), and D_u (g)-(h). Vertical green dashed lines indicate parallel and perpendicular integral scales k_{\parallel}^{int} and k_{\perp}^{int} , while horizontal green dashed lines represent the nonlinear time τ_{nl} .

terms can be rewritten as

$$\begin{aligned}
 W_P &= \langle -\bar{P} \nabla \cdot \hat{\mathbf{u}} \rangle, & D_u &= \langle \bar{\Pi} : \nabla \hat{\mathbf{u}} \rangle, \\
 \Pi_u &= \langle -\bar{\rho} \tau_u : \nabla \hat{\mathbf{u}} - \tau_B \cdot \hat{\mathbf{u}} \rangle, & & (15) \\
 \Pi_B &= \langle \tau_E \cdot \bar{\mathbf{J}} \rangle, & D_B &= \langle \eta \bar{\mathbf{J}}^2 \rangle.
 \end{aligned}$$

Magnetic and kinetic injection and dissipation rates

In this section, we show the energy injection rate and the energy dissipation rate decomposed into their magnetic and kinetic components, for the $(\beta = 0.5, \sigma_c \simeq 0)$ simulation analyzed in the Letter.

The first row of Fig. 4 shows the magnetic energy injection rate I_B , panels (a)-(b), and the kinetic energy injection rate I_u , panels (c)-(d). Both terms exhibit a similar $(k_{\perp}, k_{\parallel}, \tau)$ dependence, with comparable amplitudes. In particular, both I_B and I_u are positive and increase with wavenumber, up to $k_{\parallel} \simeq 1.3$ and $k_{\perp} \simeq 6$, after which they saturates as there is no contribution stemming from larger wavenumbers. I_B and I_u increase from $\tau \simeq 15$ to $\tau \simeq 1.5$, being almost constant elsewhere. The fact that I_B and I_u have analogous features, including a broadband frequency response, is a consequence of the design of our turbulent drivers \mathbf{F}_B and \mathbf{F}_u , both of them injecting magnetic and velocity fluctuations in the

same range of wavenumbers and frequencies, with similar amplitudes.

The energy dissipation rate components are shown in the second row of Fig. 4, where D_B is the magnetic energy dissipation rate, panels (e)-(f), and D_u is the kinetic energy dissipation rate, panels (g)-(h). Both D_B and D_u are weak at large scales, and quickly increase toward large wavenumbers and small τ . This behavior implies that dissipation affects mainly large wavenumbers and high frequencies, while low ω fluctuations are not dissipated. The similarities observed for D_B and D_u are a consequence of the fact that we have chosen both the viscosity ν and magnetic diffusivity η to have the same value.

Imbalanced turbulence run and high- β run

In this section, we show results from our spatio-temporal coarse graining (CG) analysis applied to other two 3D magnetohydrodynamic (MHD) simulations of turbulence, realized using the code *Athena++*. Both simulations are initialized with exactly the same parameters as the simulation analyzed in the Letter, but we vary the cross helicity and plasma β . Cross helicity σ_c is defined

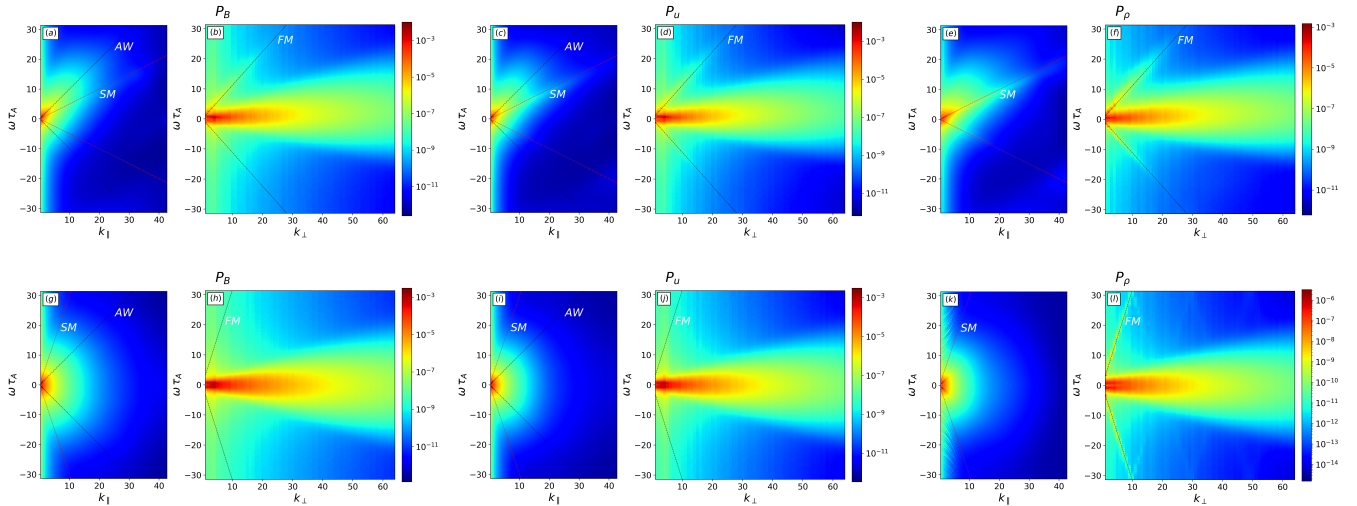


FIG. 5. (k_{\parallel}, ω) and (k_{\perp}, ω) projections of magnetic field, velocity and density spectra P_B , P_u and P_{ρ} for the imbalanced turbulence run (a)-(f), and for the high- β turbulence run (g)-(l). Dashed lines indicate the dispersion relations of Alfvén wave (AW) and slow modes (SM) for parallel propagation ($k_{\perp} = 0$), and of fast modes (FM) for perpendicular propagation ($k_{\parallel} = 0$).

as

$$\sigma_c = \frac{2\sqrt{\rho}\mathbf{u} \cdot \delta\mathbf{B}}{\rho u^2 + \delta B^2}, \quad (16)$$

where $\delta\mathbf{B} = \mathbf{B} - \mathbf{B}_0$ (with $\mathbf{B}_0 = B_0 \hat{\mathbf{z}}$ being the guide field). The first simulation (run A) has ($\beta = 0.5$, $\sigma_c \simeq 0.73$), representing near-Sun solar wind turbulence, where σ_c reaches large values [78]. The second simulation (run B) has ($\beta = 18$, $\sigma_c \simeq 0$), typical of solar wind turbulence in the outer heliosphere [77]. Due to the different σ_c and β , both simulations reach a fully developed state where magnetic, velocity and density fluctuations exhibit root mean square (rms) amplitudes slightly different from the simulation analyzed in the Letter. Specifically, run A has $\delta B_{rms}/B_0 \simeq 0.17$ and $\delta u_{rms}/c_A \simeq 0.17$ (with c_A being the Alfvén speed), while run B has $\delta B_{rms}/B_0 \simeq 0.15$ and $\delta u_{rms}/c_A \simeq 0.14$. Density fluctuations reach an rms amplitude of $\delta\rho_{rms}/\rho_0 \simeq 0.06$ (with ρ_0 being the initial density) in run A, while run B has $\delta\rho_{rms}/\rho_0 \simeq 0.003$, due to high β suppressing compressible fluctuations [74].

Figure 5 shows (k_{\parallel}, ω) and (k_{\perp}, ω) projections of magnetic field, velocity and density spectra P_B , P_u and P_{ρ} , for run A, panels (a)-(f), and for run B, panels (g)-(l), with dashed lines indicating dispersion relations of Alfvén waves (AW), slow modes (SM), and fast modes (FM). We see that in both runs, most of magnetic and kinetic energy is concentrated at low ω and small k_{\parallel} , with a wider distribution in k_{\perp} , and only a negligible fraction of energy associated with waves. This is analogous to what we observe in the ($\beta = 0.5$, $\sigma_c \simeq 0$) simulation analyzed in the Letter. Density spectra exhibit a similar distribution as P_B and P_u in $(k_{\parallel}, k_{\perp}, \omega)$ space, with P_{ρ} being about three orders of magnitude smaller in run B with respect

to run A, consistently with the lower level of compressibility expected for high β turbulence. A regular wavy pattern is observed in the (k_{\parallel}, ω) projection of P_{ρ} , at small k_{\parallel} and toward high ω , in run B. This pattern is caused by the finite energy contained in FMs, producing those features in (k_{\parallel}, ω) space when averaged over k_{\perp} . A peculiar property of run A is that all spectra are skewed toward positive ω in (k_{\parallel}, ω) space. This happens because high σ_c implies that modes propagating in the direction parallel to the guide field \mathbf{B}_0 have less energy than modes propagating antiparallel to \mathbf{B}_0 [75].

Figure 6 shows (k_{\parallel}, τ) and (k_{\perp}, τ) projections of the magnetic energy cascade rate Π_B , electromagnetic (e.m.) work $W_{e.m.}$, and kinetic energy cascade rate Π_u , for run A, panels (a)-(f), and for run B, panels (g)-(l), with black lines indicating their isocontours. As a reference, we show the parallel and perpendicular integral scales k_{\parallel}^{int} and k_{\perp}^{int} (horizontal green dashed lines), together with the nonlinear time τ_{nl} (vertical green dashed lines), as defined in the Letter. Since runs A and B are driven with the same method as the simulation analyzed in the Letter, with the same viscosity ν and magnetic diffusivity η , energy injection rates I_B and I_u , and energy dissipation rates D_B and D_u , exhibit the same properties as those of the ($\beta = 0.5$, $\sigma_c \simeq 0$) run, so we do not show them here, to avoid redundancy. The pressure work W_p , quantifying compressible effects, is negligibly small with respect to the other energy transfer channels (ETCs) in both simulations (especially in run B). Hence, we do not show W_p for runs A and B here, since its contribution to the global energy balance is irrelevant. Here, we focus on analyzing Π_B , $W_{e.m.}$ and Π_u , as their interplay

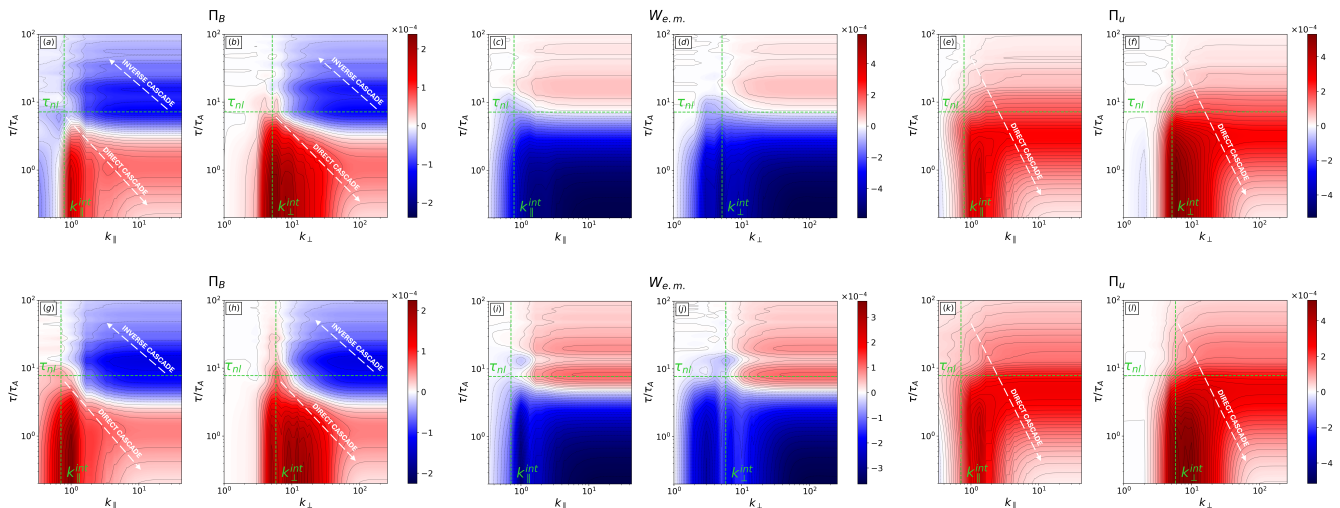


FIG. 6. (k_{\parallel}, τ) and (k_{\perp}, τ) projections of Π_B , $W_{e.m.}$ and Π_u for the imbalanced turbulence run (a)-(f), and for the high- β turbulence run (g)-(l). Vertical green dashed lines indicate parallel and perpendicular integral scales k_{\parallel}^{int} and k_{\perp}^{int} , while horizontal green dashed lines represent the nonlinear time τ_{nl} .

is responsible for the origin of low ω fluctuations and for their contribution to the turbulent cascade. Figures 6(a)-(b) show that Π_B of run A has a bifurcation in τ space, being negative (inverse cascade) for $\tau \gtrsim \tau_{nl}$, and positive (direct cascade) for $\tau < \tau_{nl}$, where it peaks around integral scales. The same kind of behavior is observed for Π_B of run B, Fig. 6(g)-(h). Thus, consistently with the ($\beta = 0.5$, $\sigma_c \simeq 0$) run analyzed in the Letter, we find that the inverse magnetic energy cascade responsible for the formation of low ω (large τ) magnetic fluctuations takes place in both imbalanced and high β turbulence. In both simulations, magnetic energy flowing to large τ is converted into low ω kinetic energy by $W_{e.m.}$, which is positive for $\tau \gtrsim \tau_{nl}$, as seen in Fig. 6(c)-(d) for run A, and in Fig. 6(i)-(j) for run B. Finally, in both runs, low ω kinetic energy cascades to small spatial and temporal scales, as highlighted by Π_u , which is positive at all (k, τ) scales, with a stronger cascade rate around k_{\parallel}^{int} , k_{\perp}^{int} and τ_{nl} , as shown in Fig. 6(e)-(f) for run A, and in Fig. 6(k)-(l) for run B. Part of the kinetic energy transferred to small scales is then converted into magnetic energy by $W_{e.m.}$, being negative for $\tau < \tau_{nl}$.

To summarize, we find that magnetic, velocity and density fluctuations in both imbalanced and high β turbulence mainly reside in low ω modes, with wavenumbers almost perpendicular to the guide field. The ETCs analysis reveals that low ω magnetic modes are produced by an inverse magnetic energy cascade affecting fluctuations with time scales $\tau \gtrsim \tau_{nl}$. Low ω magnetic modes transfer part of their energy to low ω velocity fluctuations, explaining the abundance of kinetic energy at low ω in energy spectra. Low ω velocity fluctuations ultimately undergo a direct cascade toward higher wavenumbers

and frequencies, meaning that low ω modes actually contribute to driving the turbulent cascade. This dynamics is consistent with what we find for the ($\beta = 0.5$, $\sigma_c \simeq 0$) simulation.

Our analysis shows that the inverse low frequency magnetic field energy cascade, which is the main finding uncovered by our spatio-temporal CG method, appears to be a robust feature of plasma turbulence, observed in both balanced and imbalanced turbulence, and for both low and high β . We finally note that in both run A and run B, $W_{e.m.}$ at large τ is weaker in amplitude than $W_{e.m.}$ of the simulation analyzed in the Letter, especially in the imbalanced case. In run A, this may be caused by the fact that, due to the MHD conservation of σ_c , imbalanced turbulence tends toward an equilibrium state where \mathbf{u} is parallel to \mathbf{B} , an effect known as “dynamic alignment”. Consequently, since the e.m. work is proportional to $\mathbf{u} \times \mathbf{B}$, dynamic alignment may weaken $W_{e.m.}$, especially at low ω as these are associated with long-lived, near-equilibrium structures. In the case of run B, the large β implies that the kinetic pressure is much larger than the magnetic pressure. As a consequence, pressure forces may dominate over e.m. forces, especially in low frequency, near-equilibrium structures, possibly explaining why $W_{e.m.}$ is weaker at large τ in the large β case.

-
- [1] R. Bruno and V. Carbone, Living Reviews in Solar Physics **10**, 2 (2013).
 - [2] J. Armstrong, B. Rickett, and S. Spangler, Astrophysical Journal, Part 1 (ISSN 0004-637X), vol. 443, no. 1, p. 209-221 **443**, 209 (1995).
 - [3] S. A. Balbus and J. F. Hawley, Reviews of modern physics

- 70**, 1 (1998).
- [4] I. Zhuravleva, E. Churazov, A. Schekochihin, S. Allen, P. Arévalo, A. Fabian, W. Forman, J. Sanders, A. Simionescu, R. Sunyaev, *et al.*, *Nature* **515**, 85 (2014).
 - [5] J. V. Shebalin, W. H. Matthaeus, and D. Montgomery, *Journal of plasma physics* **29**, 525 (1983).
 - [6] P. Goldreich and S. Sridhar, *Astrophysical Journal, Part 1* (ISSN 0004-637X), vol. 438, no. 2, p. 763-775 **438**, 763 (1995).
 - [7] J. Cho and E. T. Vishniac, *The Astrophysical Journal* **539**, 273 (2000).
 - [8] T. S. Horbury, M. Forman, and S. Oughton, *Physical Review Letters* **101**, 175005 (2008).
 - [9] R. Wicks, T. Horbury, C. Chen, and A. Schekochihin, *Monthly Notices of the Royal Astronomical Society: Letters* **407**, L31 (2010).
 - [10] S. S. Cerri, D. Grošelj, and L. Franci, *Frontiers in Astronomy and Space Sciences* **6**, 64 (2019).
 - [11] S. Oughton and W. H. Matthaeus, *The Astrophysical Journal* **897**, 37 (2020).
 - [12] T. Parashar, S. Servidio, B. Breech, M. Shay, and W. Matthaeus, *Physics of Plasmas* **17** (2010).
 - [13] S. Markovskii and B. J. Vasquez, *The Astrophysical Journal* **903**, 80 (2020).
 - [14] E. Papini, A. Cicone, L. Franci, M. Piersanti, S. Landi, P. Hellinger, and A. Verdini, *The Astrophysical Journal Letters* **917**, L12 (2021).
 - [15] X. Fu, H. Li, Z. Gan, S. Du, and J. Steinberg, *The Astrophysical Journal* **936**, 127 (2022).
 - [16] Z. Gan, H. Li, X. Fu, and S. Du, *The Astrophysical Journal* **926**, 222 (2022).
 - [17] Y. Narita, F. Sahraoui, M. Goldstein, and K.-H. Glassmeier, *Journal of Geophysical Research: Space Physics* **115** (2010).
 - [18] L.-L. Zhao, G. Zank, M. Nakanotani, and L. Adhikari, *The Astrophysical Journal* **944**, 98 (2023).
 - [19] O. Alexandrova, *Nonlinear Processes in Geophysics* **15**, 95 (2008).
 - [20] S. Lion, O. Alexandrova, and A. Zaslavsky, *The Astrophysical Journal* **824**, 47 (2016).
 - [21] G. Zank, L.-L. Zhao, L. Adhikari, D. Telloni, J. Kasper, and S. Bale, *Physics of Plasmas* **28** (2021).
 - [22] G. Arrò, F. Pucci, F. Califano, M. E. Innocenti, and G. Lapenta, *The Astrophysical Journal* **958**, 11 (2023).
 - [23] G. Arrò, F. Califano, F. Pucci, T. Karlsson, and H. Li, *The Astrophysical Journal Letters* **970**, L6 (2024).
 - [24] G. P. Zank, L.-L. Zhao, L. Adhikari, D. Telloni, P. Baruwal, P. Baruwal, X. Zhu, M. Nakanotani, A. Pitňa, J. C. Kasper, *et al.*, *The Astrophysical Journal* **966**, 75 (2024).
 - [25] W. H. Matthaeus, M. L. Goldstein, and D. A. Roberts, *Journal of Geophysical Research: Space Physics* **95**, 20673 (1990).
 - [26] G. Zank and W. Matthaeus, *Journal of geophysical research* **97**, 17189 (1992).
 - [27] G. Zank, A. Dosch, P. Hunana, V. Florinski, W. Matthaeus, and G. Webb, *The Astrophysical Journal* **745**, 35 (2011).
 - [28] C. Ng and A. Bhattacharjee, *Astrophysical Journal v.* 465, p. 845 **465**, 845 (1996).
 - [29] S. Galtier, S. Nazarenko, A. C. Newell, and A. Pouquet, *Journal of plasma physics* **63**, 447 (2000).
 - [30] P. Dmitruk and W. Matthaeus, *Physics of Plasmas* **16** (2009).
 - [31] K. H. Yuen, H. Li, and H. Yan, arXiv preprint arXiv:2310.03806 (2023).
 - [32] P. Dmitruk and W. Matthaeus, *Physical Review E* **76**, 036305 (2007).
 - [33] P. Dmitruk, P. D. Mininni, A. Pouquet, S. Servidio, and W. Matthaeus, *Physical Review E* **83**, 066318 (2011).
 - [34] W. H. Matthaeus, G. P. Zank, S. Oughton, D. Mullan, and P. Dmitruk, *The Astrophysical Journal* **523**, L93 (1999).
 - [35] P. Dmitruk, W. H. Matthaeus, L. Milano, S. Oughton, G. P. Zank, and D. Mullan, *The Astrophysical Journal* **575**, 571 (2002).
 - [36] S. R. Cranmer, A. A. Van Ballegooijen, and R. J. Edgar, *The Astrophysical Journal Supplement Series* **171**, 520 (2007).
 - [37] S. R. Cranmer, M. Asgari-Targhi, M. P. Miralles, J. C. Raymond, L. Strachan, H. Tian, and L. N. Woolsey, *Philosophical Transactions of the Royal Society A: Mathematical, Physical and Engineering Sciences* **373**, 20140148 (2015).
 - [38] W. Matthaeus and M. Goldstein, *Physical review letters* **57**, 495 (1986).
 - [39] W. Matthaeus, B. Breech, P. Dmitruk, A. Bemporad, G. Poletto, M. Velli, and M. Romoli, *The Astrophysical Journal* **657**, L121 (2007).
 - [40] J. Giacalone and J. Jokipii, *The astrophysical journal* **520**, 204 (1999).
 - [41] H. Yan and A. Lazarian, *Physical review letters* **89**, 281102 (2002).
 - [42] H. Yan and A. Lazarian, *The Astrophysical Journal* **614**, 757 (2004).
 - [43] H. H. Klahr and P. Bodenheimer, *The Astrophysical Journal* **582**, 869 (2003).
 - [44] T. Sano, S.-i. Inutsuka, N. J. Turner, and J. M. Stone, *The Astrophysical Journal* **605**, 321 (2004).
 - [45] R. B. Larson, *Monthly Notices of the Royal Astronomical Society* **194**, 809 (1981).
 - [46] N. Schneider, S. Bontemps, R. Simon, V. Ossenkopf, C. Federrath, R. S. Klessen, F. Motte, P. André, J. Stutzki, and C. Brunt, *Astronomy & Astrophysics* **529**, A1 (2011).
 - [47] A. A. Schekochihin, S. C. Cowley, S. F. Taylor, J. L. Maron, and J. C. McWilliams, *The Astrophysical Journal* **612**, 276 (2004).
 - [48] Y. Ponty, H. Politano, and J.-F. Pinton, *Physical Review Letters* **92**, 144503 (2004).
 - [49] A. Beresnyak, *Physical Review Letters* **108**, 035002 (2012).
 - [50] G. L. Eyink and H. Aluie, *Physics of Fluids* **21** (2009).
 - [51] H. Aluie, S. Li, and H. Li, *The Astrophysical Journal Letters* **751**, L29 (2012).
 - [52] A. Mondal, A. J. Morten, B. K. Arbic, G. R. Flierl, R. B. Scott, and J. Skitka, arXiv preprint arXiv:2405.02259 (2024).
 - [53] H. Aluie and G. L. Eyink, *Physical review letters* **104**, 081101 (2010).
 - [54] H. Aluie, *Physica D: Nonlinear Phenomena* **247**, 54 (2013).
 - [55] Y. Yang, Y. Shi, M. Wan, W. H. Matthaeus, and S. Chen, *Physical Review E* **93**, 061102 (2016).
 - [56] Y. Yang, W. H. Matthaeus, T. N. Parashar, C. C. Haggerty, V. Roytershteyn, W. Daughton, M. Wan, Y. Shi, and S. Chen, *Physics of Plasmas* **24** (2017).
 - [57] Y. Yang, W. H. Matthaeus, Y. Shi, M. Wan, and S. Chen,

- Physics of Fluids **29** (2017).
- [58] W. H. Matthaeus, Y. Yang, M. Wan, T. N. Parashar, R. Bandyopadhyay, A. Chasapis, O. Pezzi, and F. Valentini, *The Astrophysical Journal* **891**, 101 (2020).
- [59] G. Arrò, F. Califano, and G. Lapenta, *Astronomy & Astrophysics* **668**, A33 (2022).
- [60] A. Favre, *Soc. Indust.*, 231 (1969).
- [61] G. L. Eyink, *Journal of Fluid Mechanics* **549**, 159 (2006).
- [62] J. M. Stone, K. Tomida, C. J. White, and K. G. Felker, *The Astrophysical Journal Supplement Series* **249**, 4 (2020).
- [63] J. TenBarge, G. G. Howes, W. Dorland, and G. W. Hammett, *Computer Physics Communications* **185**, 578 (2014).
- [64] R. Bandyopadhyay, L. Sorriso-Valvo, A. Chasapis, P. Hellinger, W. H. Matthaeus, A. Verdini, S. Landi, L. Franci, L. Matteini, B. L. Giles, *et al.*, *Physical review letters* **124**, 225101 (2020).
- [65] S. Du, H. Li, X. Fu, and Z. Gan, *The Astrophysical Journal* **948**, 72 (2023).
- [66] P. Hellinger, A. Verdini, V. Montagnud-Camps, L. Franci, E. Papini, L. Matteini, and S. Landi, *Astronomy & Astrophysics* **684**, A120 (2024).
- [67] V. Eswaran and S. B. Pope, *Computers & Fluids* **16**, 257 (1988).
- [68] J. TenBarge and G. Howes, *Physics of Plasmas* **19** (2012).
- [69] U. Frisch, *Turbulence: the legacy of AN Kolmogorov* (Cambridge university press, 1995).
- [70] O. Alexandrova, C. H. Chen, L. Sorriso-Valvo, T. S. Horbury, and S. D. Bale, *Space Science Reviews* **178**, 101 (2013).
- [71] J. Squire, R. Meyrand, M. W. Kunz, L. Arzamasskiy, A. A. Schekochihin, and E. Quataert, *Nature Astronomy* **6**, 715 (2022).
- [72] E. Papini, L. Franci, S. Landi, A. Verdini, L. Matteini, and P. Hellinger, *The Astrophysical Journal* **870**, 52 (2019).
- [73] G. Arrò, F. Califano, and G. Lapenta, *Astronomy & Astrophysics* **642**, A45 (2020).
- [74] D. Biskamp and D. Biskamp, *Nonlinear magnetohydrodynamics*, 1 (Cambridge University Press, 1997).
- [75] R. Lugones, P. Dmitruk, P. D. Mininni, A. Pouquet, and W. H. Matthaeus, *Physics of Plasmas* **26** (2019).
- [76] A. A. Schekochihin, *Journal of Plasma Physics* **88**, 155880501 (2022).
- [77] F. Fraternali, L. Zhao, N. V. Pogorelov, L. Sorriso-Valvo, S. Redfield, M. Zhang, K. Ghanbari, V. Florinski, and T. Y. Chen, *Frontiers in Astronomy and Space Sciences* **9**, 1064098 (2022).
- [78] C. Chen, S. Bale, J. Bonnell, D. Borovikov, T. Bowen, D. Burgess, A. Case, B. Chandran, T. D. de Wit, K. Goetz, *et al.*, *The Astrophysical Journal Supplement Series* **246**, 53 (2020).
- [79] U. Frisch, A. Pouquet, J. Léorat, and A. Mazure, *Journal of Fluid Mechanics* **68**, 769 (1975).
- [80] A. Alexakis, P. D. Mininni, and A. Pouquet, *The Astrophysical Journal* **640**, 335 (2006).
- [81] Q. Hu and B. U. Sonnerup, *Geophysical research letters* **28**, 467 (2001).
- [82] A. Lui, *Space science reviews* **158**, 43 (2011).
- [83] F. Pecora, A. Greco, Q. Hu, S. Servidio, A. G. Chasapis, and W. H. Matthaeus, *The Astrophysical Journal Letters* **881**, L11 (2019).